Direct simulation of turbulence-chemistry interaction in a strongly reacting turbulent hypersonic boundary layer

By C. T. Williams, M. Di Renzo† AND P. Moin

1. Motivation and objectives

The conversion of bulk kinetic energy into molecular thermal motion via shock-induced compression and viscous dissipation activates a number of temperature-dependent thermochemical processes within the shock layer of high-speed flight vehicles (Urzay 2018; Urzay & Di Renzo 2020). These high-enthalpy effects include the activation of additional internal degrees of freedom in the form of vibrational and electronic excitation, together with the initiation of chemical reactions among the atomic and molecular components of high-temperature air (Vincenti & Kruger 1965; Park 1990). Owing to the comparable characteristic timescales of hydrodynamic motion and thermochemical relaxation in hypersonic flows, the composition within high-Mach boundary layers cannot generally be equated to the maximum-entropy chemical configuration corresponding to the local pressure and internal energy (Candler 2019). Due to this thermochemical non-equilibrium, the local chemical composition intrinsically depends on the relative rates of advective transport and chemical production, even in the limit of laminar hypersonic boundary layers (Liñán & Da Riva 1962; Seror *et al.* 1997; Williams *et al.* 2021). This coupling between the hydrodynamic and thermochemical fields is then further complicated by the introduction of a multiplicity of hydrodynamic timescales upon breakdown to turbulence, with turbulent fluctuations in thermodynamic state variables directly modulating the rates of the aforementioned non-equilibrium thermochemical processes.

Interactions between wall-bounded turbulence and hypersonic aerothermochemistry were first characterized by Martín & Candler (2001), who quantified the sensitive coupling between thermal and compositional fluctuations in a temporally evolving boundary layer. Utilizing more realistic chemical mechanisms, subsequent efforts by Duan & Martin (2011a,b) confirmed that turbulence-induced fluctuations in the thermodynamic state variables significantly modify chemical production rates in hypersonic boundary layers, introducing the interaction Damköhler number as the relevant controlling parameter. Most recently, Di Renzo & Urzay (2021) incorporated the effects of spatial evolution in their numerical simulation of a transitional/turbulent hypersonic boundary layer with finite-rate chemistry, observing, however, only limited chemical activity due to the moderate temperatures attained in the aerodynamic heating layer. In order to further elucidate the nature of turbulence-aerothermochemistry interactions, then, the present study introduces direct numerical simulation results for a strongly reacting, spatially evolving hypersonic boundary layer for which the chemical reactions and hydrodynamic turbulence evolve on comparable timescales.

The remainder of this brief is structured as follows. Section 2 introduces the relevant conservation equations together with the treatment of molecular transport and chemical

† University of Salento, Italy & CTR

kinetics employed for the present study. The computational methodology utilized for the direct numerical simulation is briefly outlined in Section 3, while the corresponding mean-flow results for the boundary-layer simulation are presented in Section 4. Finally, Section 5 draws conclusions and identifies directions for further research.

2. Formulation

2.1. *Conservation equations*

On account of the finite-rate evolution of the chemical state variables in hypersonic flows, determination of the local composition entails integration of a partial density conservation equation for each of the components. In the standard formulation of multi-component reacting hypersonic flows, the species conservation equations can be expressed compactly as

$$\frac{\partial(\rho Y_i)}{\partial t} + \nabla\cdot(\rho Y_i \mathbf{u}) = -\nabla\cdot(\rho Y_i \boldsymbol{V_i}) + \dot{w}_i \qquad i = 1, ..., N_s, \tag{2.1}$$

where ρ and $\mathbf{u} = [u,\ v,\ w]^T$ are the overall density and mass-averaged velocity of the reacting mixture, respectively. The mass fraction for a given species i is denoted by Y_i, whereas $\boldsymbol{V_i}$ is defined as the corresponding diffusion velocity, and $\dot{w}_i$ is taken to be the net chemical production rate per unit volume. The diffusion velocities are determined following Curtiss & Hirschfelder (1949) as

$$\boldsymbol{V_i} = -D_i \nabla \ln X_i + \sum_{j=1}^{N_s} Y_j D_j \nabla \ln X_i, \tag{2.2}$$

where $X_i = \overline{\mathcal{M}} Y_i / \mathcal{M}_i$ and D_i respectively correspond to the molar fraction of, and to the mixture-averaged mass diffusivity (Bird *et al.* 1960) for, species i. In this formulation, the molar mass of species i is given by $\mathcal{M}_i$, whereas $\overline{\mathcal{M}} = [\sum_{i=1}^{N_s} Y_i/\mathcal{M}_i]^{-1}$ denotes the effective molecular weight of the mixture. The present study utilizes the Park (1990) chemical mechanism for air dissociation given by

$$\mathrm{N_2 + M \rightleftharpoons 2N + M}, \tag{R1}$$
$$\mathrm{O_2 + M \rightleftharpoons 2O + M}, \tag{R2}$$
$$\mathrm{NO + M \rightleftharpoons N + O + M}, \tag{R3}$$
$$\mathrm{N_2 + O \rightleftharpoons NO + N}, \tag{R4}$$
$$\mathrm{NO + O \rightleftharpoons O_2 + N}. \tag{R5}$$

This mechanism comprises the dissociation/recombination reactions for each of the diatomic species species given by (R1)-(R3), supplemented by the Zel'dovich exchange reactions, (R4) and (R5). The reactive mixture itself is composed of five neutral species, i.e., $N_s = 5$, with the symbolic species M representing the third-body collision partners entering into the dissociation/recombination reactions. As such, accounting for all collision partners, the total number of reactions considered is $N_r = 17$. Following from the law of mass action, the net chemical production term for species i can then be evaluated with

$$\dot{w}_i = \mathcal{M}_i \sum_{j=R1}^{R5} (\nu''_{ij} - \nu'_{ij}) \sum_{l=1}^{N_s} F_{lj} \left[k_{f,j} \prod_{k=1}^{N_s} \left(\frac{\rho Y_k}{\mathcal{M}_k} \right)^{\nu'_{kj}} - k_{b,j} \prod_{k=1}^{N_s} \left(\frac{\rho Y_k}{\mathcal{M}_k} \right)^{\nu''_{kj}} \right], \tag{2.3}$$

where F_{lj} is the chaperon efficiency of the third-body collision partner l in reaction j, while $\nu'_{kj}, \nu''_{kj} \in \mathbb{N}$ respectively correspond to the forward and reverse stoichiometric coefficients for species k in elementary reaction j. The modified-Arrhenius rate constants for each of the reactions in the forward direction are given by

$$k_{f,j} = A_j T^{m_j} \exp\left(-\frac{E_{a,j}}{\mathrm{R}^0 T}\right), \qquad j = 1, ..., N_r, \tag{2.4}$$

where R^0 denotes the universal gas constant, and A_j, m_j, and $E_{a,j}$ are the Arrhenius parameters provided by Park (1989). The rate constants for each of the backward reactions are likewise computed via

$$k_{b,j} = \frac{A_j T^{m_j}}{K_{eq,j}} \exp\left(-\frac{E_{a,j}}{\mathrm{R}^0 T}\right), \qquad j = 1, ..., N_r. \tag{2.5}$$

Appealing to equilibrium statistical mechanics, the chemical equilibrium constants $K_{eq,j}$ are evaluated with

$$K_{eq,j} = \exp\left(-\sum_{k=1}^{N_s} (\nu''_{kj} - \nu'_{kj}) \frac{\mathcal{G}_k}{\mathrm{R}^0 T}\right) \left(\frac{P_0}{\mathrm{R}^0 T}\right)^{\sum_{i=1}^{N_s} \left(\nu''_{ij} - \nu'_{ij}\right)}, \tag{2.6}$$

where $\mathcal{G}_k$ is the Gibbs free energy of species k, evaluated at the reference pressure P_0. For the present study, the Gibbs free energy for each species is evaluated with the parameterization of McBride *et al.* (2002); therefore, P_0 is taken to be 100 kPa. The conservation of momentum implies

$$\frac{\partial(\rho \mathbf{u})}{\partial t} + \nabla \cdot (\rho \mathbf{u}\mathbf{u}) = -\nabla P + \nabla \cdot \overline{\overline{\boldsymbol{\tau}}}. \tag{2.7}$$

The ideal-gas equation of state then relates the pressure P to the thermodynamic temperature T as

$$P = \rho \mathrm{R}^0 T / \overline{\mathcal{M}}. \tag{2.8}$$

Consistent with Stokes' hypothesis, the viscous stress tensor may be expressed in terms of the strain-rate tensor $\overline{\overline{\boldsymbol{S}}} = \left(\nabla \boldsymbol{u} + \nabla \boldsymbol{u}^T\right)/2$ and identity tensor $\overline{\overline{\boldsymbol{I}}}$ as

$$\overline{\overline{\boldsymbol{\tau}}} = 2\mu \overline{\overline{\boldsymbol{S}}} - \frac{2\mu}{3} (\nabla \cdot \mathbf{u}) \overline{\overline{\boldsymbol{I}}}, \tag{2.9}$$

where μ is the dynamic viscosity of the mixture. For the present study, μ is determined from Wilke's mixture rule (Wilke 1950) for which the elementary viscosity of each species is evaluated following the approach of Curtiss & Hirschfelder (1949). The corresponding conservation equation for the total energy is

$$\frac{\partial(\rho E)}{\partial t} + \nabla \cdot (\rho E \mathbf{u}) = \nabla \cdot \left(-\mathbf{u}P + \overline{\overline{\boldsymbol{\tau}}}\mathbf{u} + \lambda \nabla T - \rho \sum_{i=1}^{N_s} Y_i \boldsymbol{V_i} h_i\right), \tag{2.10}$$

where λ is the effective thermal conductivity determined from the mixing rule of Saxena *et al.* (1967), with the thermal conductivity of each component evaluated following the approach of Peters & Warnatz (1982). The stagnation energy E comprises contributions from specific kinetic energy and internal energy as $E = (\mathbf{u} \cdot \mathbf{u})/2 + e$. The internal energy itself accounts for both excitation of thermal motion and chemical energy stored

in molecular bonds with

$$e = \sum_{i=1}^{N_s} Y_i h_i - P/\rho, \tag{2.11}$$

where h_i is the specific enthalpy of species i evaluated with the polynomial description of McBride *et al.* (2002).

3. Computational approach

The set of conservation equations formulated in the prior section is integrated numerically with the HTR solver (Di Renzo *et al.* 2020) in order to perform direct numerical simulation of a transitional/turbulent reacting hypersonic boundary layer. The inviscid fluxes are evaluated with a low-dissipation, sixth-order hybrid skew-symmetric/TENO scheme (Williams*et al.* 2022), while explicit time advancement is performed using a third-order strong-stability-preserving Runge-Kutta method. The direct numerical simulation is performed in a Cartesian computational domain with the incoming boundary-layer profile obtained from a separate two-dimensional simulation of laminar reacting hypersonic flow over a 16° wedge at a free-stream Mach number of 24.9. As such, the corresponding edge Mach number for the boundary-layer calculation is 7.0 with an edge temperature of 2686 K. The wall is treated as isothermal and non-catalytic with a temperature of 3000 K.

The computational domain for the direct numerical simulation extends a length of $800\delta_0^*, 14\pi\delta_0^*$, and $40\delta_0^*$ in the streamwise, spanwise, and wall-normal directions, respectively, where δ_0^* is the displacement thickness of the incoming laminar boundary layer. The computational domain is discretized with 11868, 1184, and 464 points in the streamwise, spanwise, and wall-normal directions, respectively, with a uniform distribution of points employed in the streamwise and spanwise coordinates. Along the wall-normal coordinate, the points are stretched as $\hat{y}_j = 40\sinh(s_y\xi_j)/\sinh(s_y)$, with $\widehat{(\cdot)}$ denoting normalization by δ_0^*. The stretching factor, s_j, is set equal to 5.0, and $\xi_j \in [0, 1]$ is a uniformly spaced computational coordinate.

Transition to turbulence is induced by suction and blowing at the wall, with the forcing applied a distance of $15\delta_0^*$ downstream of the inflow boundary. The forcing employed for the present study has the same functional form as that of Di Renzo & Urzay (2021), for which a non-zero vertical velocity is imposed at the wall. For the present study, two modes are introduced, each with an amplitude set to 5.0% of the edge streamwise velocity, U_e. The spanwise wavenumbers for the forcing modes are $\pm 2/(7\delta_0^*)$, each with a temporal frequency of $9a_e/(10\delta_0^*)$, where a_e is the speed of sound at the edge of the boundary. Finally, periodicity is enforced in the spanwise direction, while characteristic boundary conditions are applied along the outflows located at $\hat{x} = 800$ and $\hat{y} = 40$.

4. Results

In addition to significantly augmenting heat flux and wall shear stress, breakdown to turbulence in the reacting hypersonic boundary layer strongly modulates the rate of chemical reactions and compositional structure of the boundary layer. Figure 1(a) depicts the Q-criterion isosurfaces colored by the local molecular-oxygen molar fraction during the laminar-to-turbulent transition, together with contours of the normalized density gradient to visualize the radiated acoustic waves. Figure 1(b) evidences the strong

$\hat{x}$	700	735	770	805	840	875	910
Re_τ	889	947	1000	1040	1088	1134	1166
Re_{δ_2}	1966	2167	2338	2434	2544	2725	2850
Re_θ	2191	2417	2609	2710	2828	3031	3171
Ma_τ	0.20	0.20	0.20	0.20	0.20	0.19	0.19
Da_O^t	0.21	0.21	0.22	0.22	0.23	0.23	0.24
Da_N^t	0.24	0.25	0.26	0.27	0.28	0.29	0.30
Δx^+	9.66	9.48	9.37	9.28	9.19	9.07	8.98
Δz^+	5.32	5.22	5.17	5.11	5.06	5.00	4.95
Δy_w^+	0.83	0.82	0.81	0.80	0.79	0.78	0.77

TABLE 1. Dimensionless parameters at select streamwise locations based on averaged primitive variables. The friction Reynolds number is defined as $Re_\tau = \langle\rho_w\rangle u_\tau \delta_{99}/\langle\mu_w\rangle$, where δ_{99} is the local boundary-layer thickness equivalent to the height at which the Favre-averaged velocity recovers 99% of the edge streamwise velocity. The Reynolds numbers based on the momentum thickness θ are likewise defined as $Re_{\delta_2} = \rho_e U_e \theta/\mu_e$ and $Re_\theta = \rho_e U_e \theta/\mu_w$. The friction Mach number is defined as $Ma_t = u_\tau/\langle a_w\rangle$, where $\langle a_w\rangle$ is the mean speed of sound evaluated at the wall. The turbulent Damköhler numbers, $Da_i^t = \max_{y^*}(|\dot{w}_i/\rho|)\delta_{99}/u_\tau$, characterize the relative rates of turbulent motion to chemical processes. Finally, the grid spacing in friction units for the streamwise and spanwise directions, together with the wall-normal spacing as evaluated at the wall, is denoted by Δx^+, Δz^+, and Δy_w^+, respectively.

variation in nitric oxide concentration through the transition process, owing to the enhanced turbulent mixing between the lower-temperature largely undissociated air at the boundary-layer edge and the strongly dissociated near-wall mixture in the aerodynamic heating layer.

Table 1 provides the set of dimensionless parameters characterizing the hydrodynamics of the turbulent reacting boundary layer as a function of streamwise displacement, including the friction and momentum-thickness Reynolds numbers together with the friction Mach number. The relevance of the present direct numerical simulation for analyzing hypersonic turbulence-chemistry interaction is corroborated by the order-unity turbulent Damköhler numbers for the atomic species, which confirm that the temporal scales characterizing the chemical processes and turbulent motion are not separable. Lastly, Table 1 reports the grid spacing in friction units, with their values indicating that the dynamically relevant turbulent length scales are resolved in the present numerical simulation.

The transformed mean-velocity profiles of the turbulent reacting boundary layer are plotted against the semi-local coordinate $y^* = y(\sqrt{\langle\rho\rangle\tau_w})/\langle\mu\rangle$ in Figure 2, with the transformation of Griffin *et al.* (2021) providing much better collapse of the data to the incompressible scaling than the transformation of van Driest (1956) owing to the strong wall cooling observed in the present configuration. The mean wall-normal profiles of the temperature and density, together with their root-mean-square (r.m.s.) and Favre root-mean-square (f.r.m.s.) profiles are likewise presented in Figure 3, where, in the present notation, the Reynolds-averaging and Favre-averaging operators are denoted by $\langle\cdot\rangle$ and $\langle\cdot\rangle_f = \langle\rho(\cdot)\rangle/\langle\rho\rangle$, respectively. The temperature reaches its peak value of 5300 K at approximately $y^* \in [12, 13]$, producing the wall-cooling effects observable in the mean velocity profiles. This peak-temperature location likewise corresponds to a global mini-

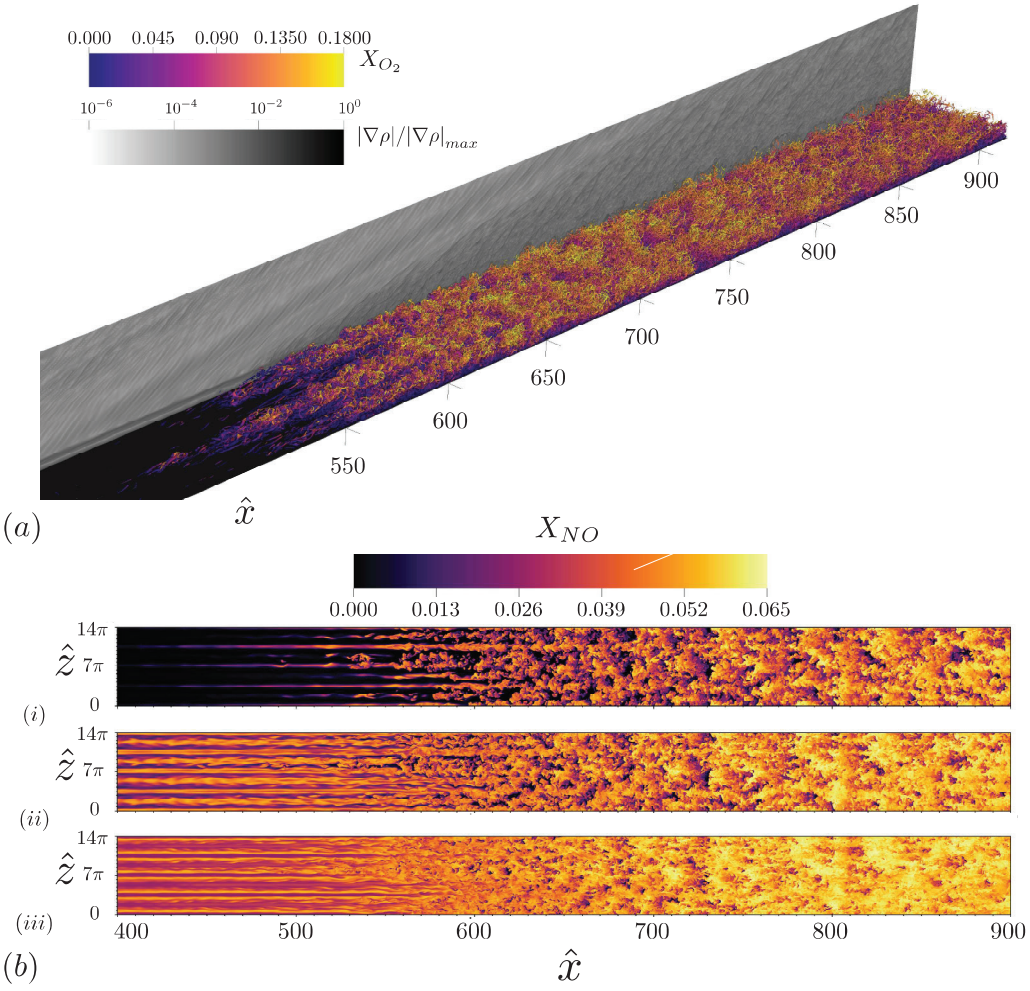

FIGURE 1. (a) Isosurface of the Q-criterion colored by the molar fraction of molecular oxygen. The side panel depicts contours of the density-gradient magnitude. (b) Instantaneous contours of the nitric oxide molar fraction at the three off-wall locations corresponding to (i) $\hat{y} = 3.0$, (ii) $\hat{y} = 2.0$, and (iii) $\hat{y} = 1.0$.

mum for the mean density and local minimum for the both the normalized temperature and density variances.

The chemical structure of the boundary layer is reported in Figures 4 and 5, which depict the wall-normal variation in the Favre-averaged molar fractions for the molecular and atomic species, respectively, juxtaposed with the corresponding Favre variances. The high temperatures generated by kinetic-energy dissipation produce strong variations in the composition with respect to wall-normal distance. Whereas the concentrations of dissociation products are negligible at the edge of the boundary layer, the molecular oxygen is almost entirely dissociated in the vicinity of the wall. Likewise, non-negligible densities of the radical species atomic nitrogen and nitric oxide are also present in the aerodynamic heating layer, with peak concentrations of approximately 6.0% and 1.0%,

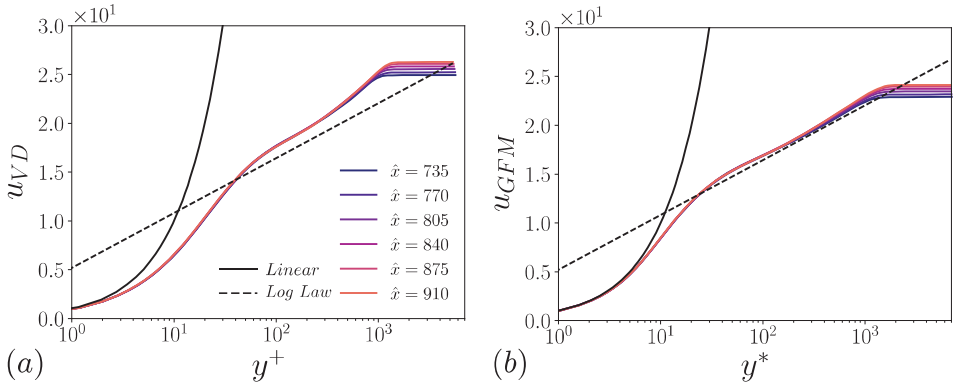

FIGURE 2. Transformed mean-velocity profiles based on the transformations introduced by (a) van Driest (1956) and (b) Griffin *et al.* (2021), together with the viscous-sublayer scaling and the incompressible law of the wall.

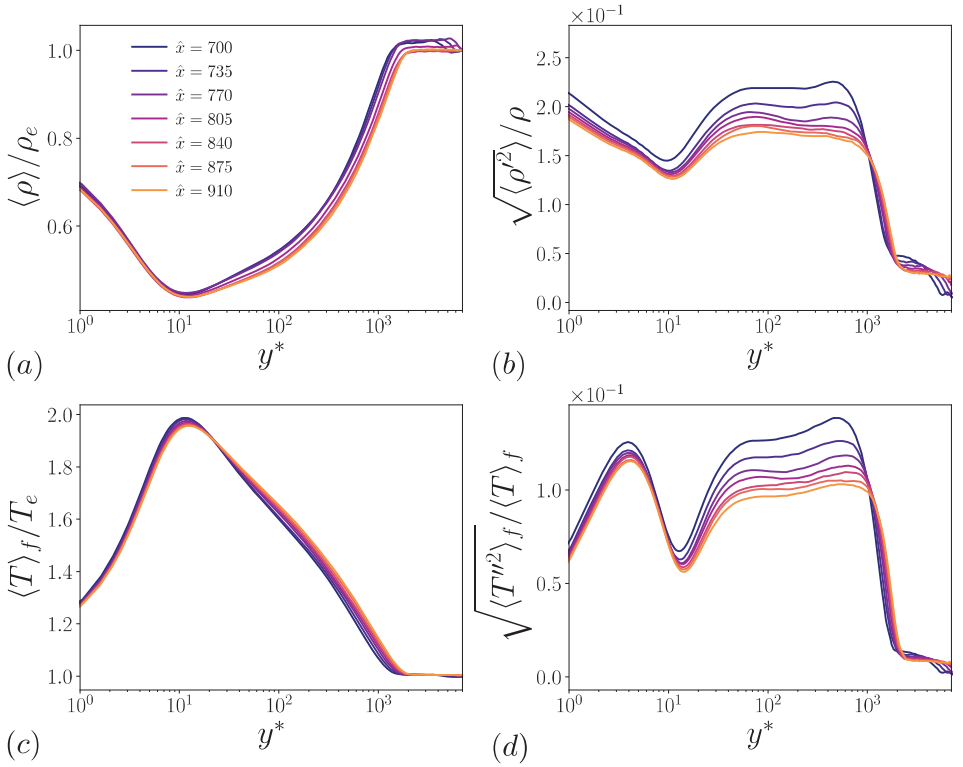

FIGURE 3. Wall-normal profiles of (a) averaged density, (b) density r.m.s., (c) Favre-averaged temperature, and (d) temperature f.r.m.s.

respectively. While the temperatures within the boundary layer are sufficiently high to produce monotonic behavior in the mean molar fractions for atomic and molecular oxygen, atomic nitrogen reaches its maximal concentration at the peak-temperature location owing to the higher activation temperature for molecular nitrogen dissociation.

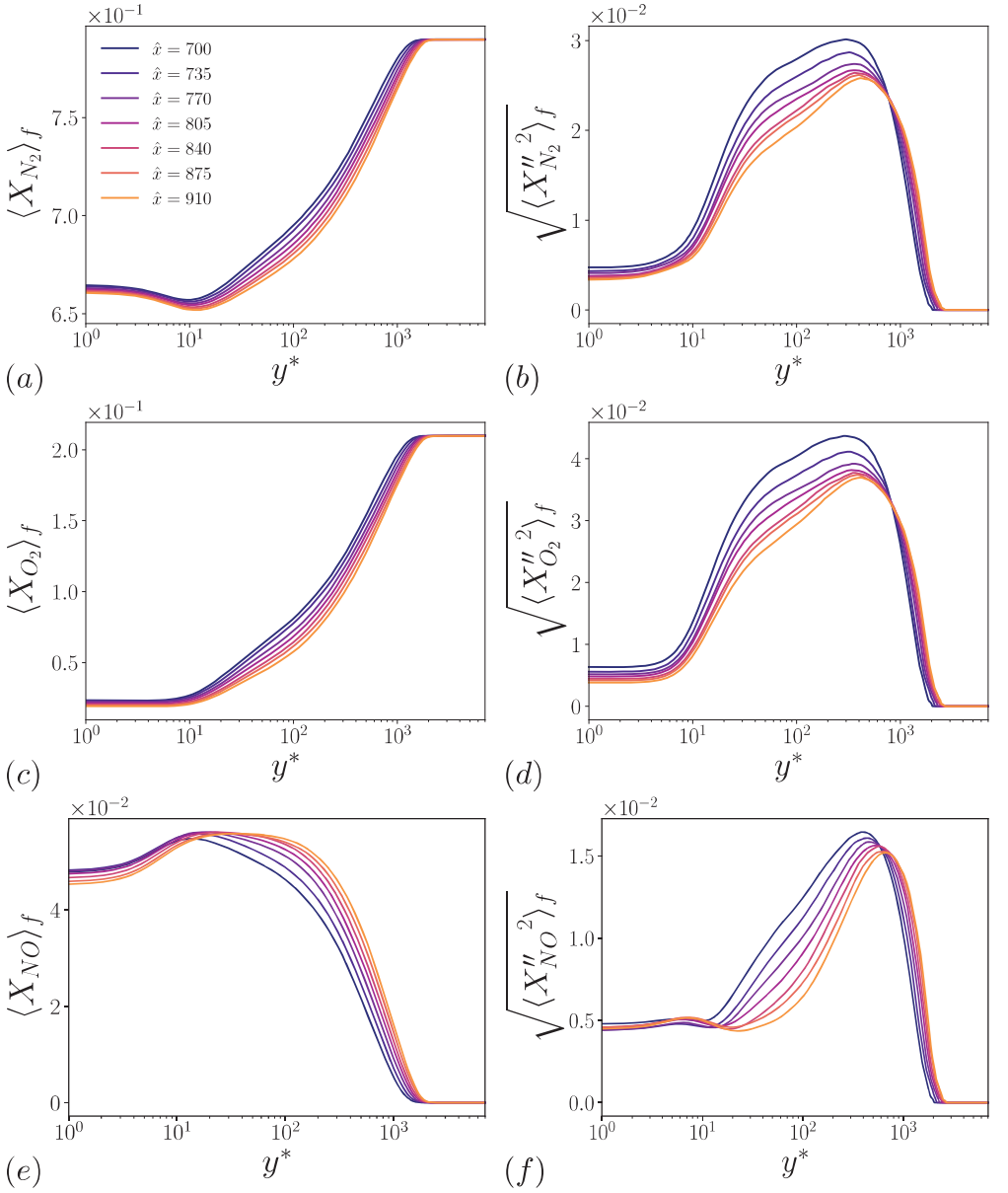

FIGURE 4. Wall-normal profiles of the Favre averages and f.r.m.s. for the molar fractions of (a, b) molecular nitrogen, (c, d) molecular oxygen, and (e, f) nitric oxide, respectively.

The mean chemical production rates, in addition to the net chemical heat release, as a function of the semi-local wall-normal coordinate are depicted in Figure 6. The chemical production rate for molecular nitrogen is clearly non-monotonic. Whereas there is net formation of molecular nitrogen occurring close to wall due to the recombination of atomic nitrogen with itself together with reactive collisions between nitric oxide with atomic nitrogen, meaningful depletion of molecular nitrogen takes place within the vicinity of the peak-temperature location. Correspondingly, while the production of nitric oxide is

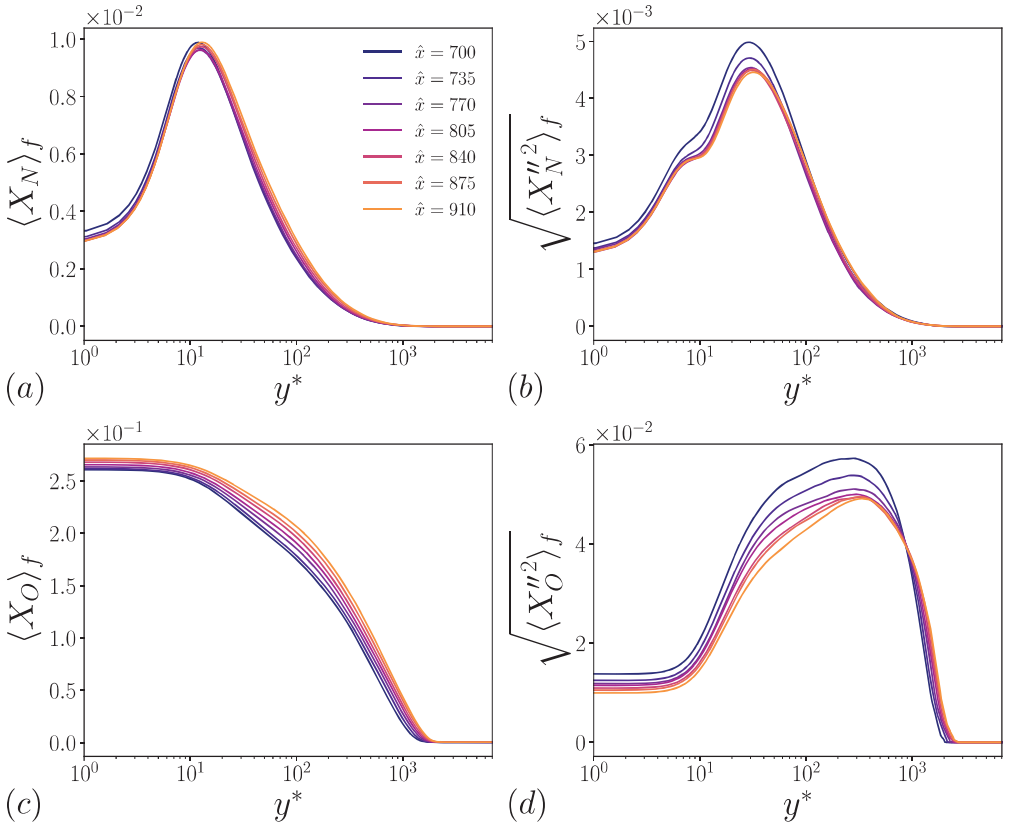

FIGURE 5. Wall-normal profiles of the Favre averages and f.r.m.s. for the molar fractions of (a, b) atomic nitrogen, and (c, d) atomic oxygen, respectively.

positive outside the temperature peak, depletion of nitric oxide predominates within the viscous sublayer. As reflected in the mean chemical concentrations, significant dissociation of molecular oxygen proceeds within the boundary layer, with the net production rate of oxygen being positive for all wall-normal locations.

However, while the net formation of molecular nitrogen is uniformly positive at the wall independent of streamwise position, the near-wall production of molecular oxygen changes sign at a given streamwise displacement corresponding approximately to $\hat{x} = 770$, after which there is a net formation of molecular oxygen at the non-catalytic wall. Naturally, due to their strong temperature dependence, the formation rates of both atomic species attain their maxima at the peak-temperature location, with the peak formation rates of both atomic radical species being comparable to the local eddy-turnover frequency.

Owing to the endothermicitiy of the dissociation reactions, the net heat release rate is negative for approximately $y^* > 5$. However within the laminar sublayer, the net rate of heat release becomes positive due to the predominance of the recombination reactions. Indeed, the magnitude of the heat release rate at the wall due to chemical activity is comparable, though obviously opposite in sign, to the heat release rate at the peak-temperature location. Moreover, the normalized heat release rate becomes increasingly

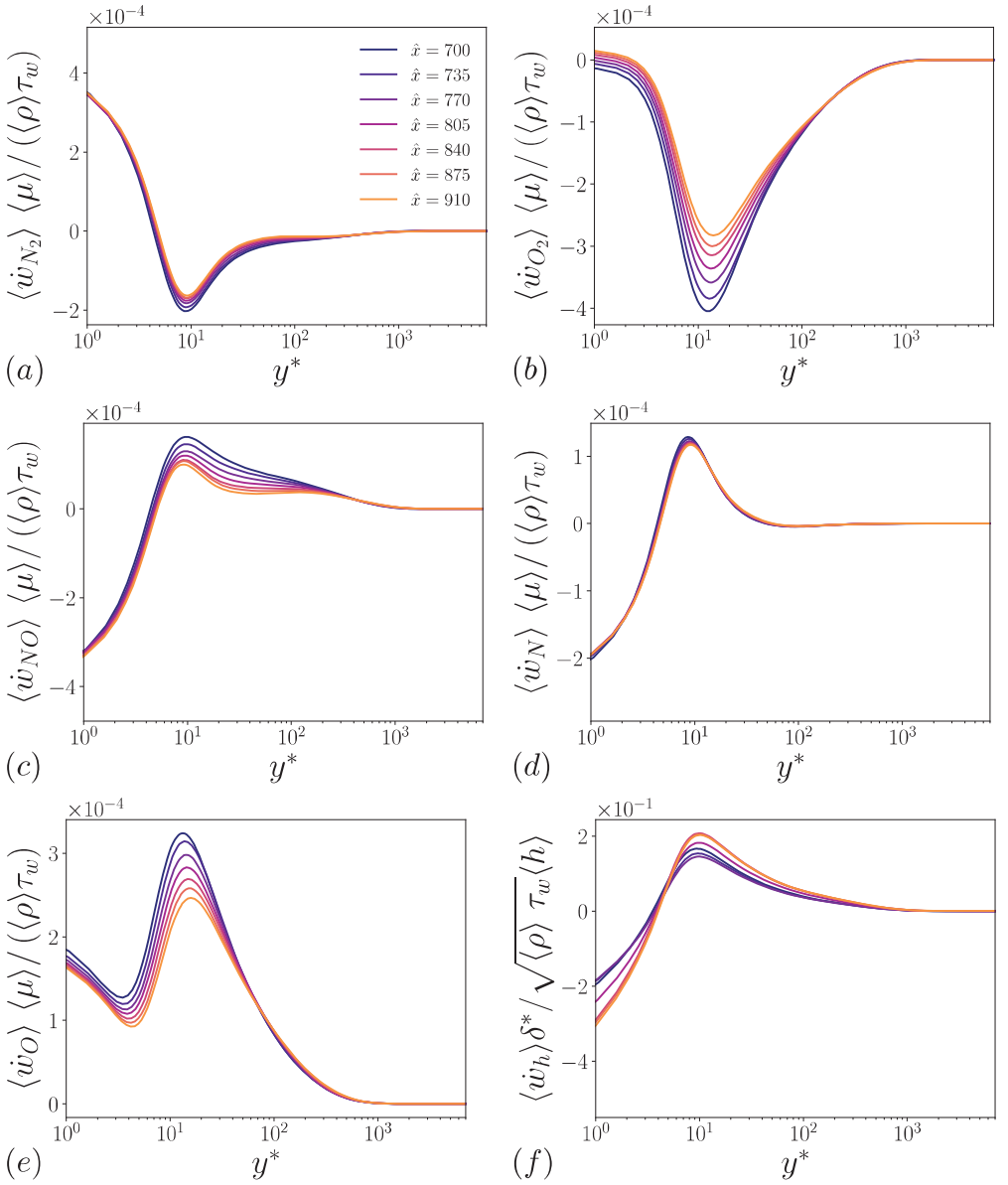

FIGURE 6. Wall-normal profiles of Reynolds-averaged net chemical production for (a) molecular nitrogen, (b) molecular oxygen, (c) nitric oxide, (d) atomic nitrogen, and (e) atomic oxygen, together with the profiles of (f) the overall heat release rate.

negative with streamwise displacement in the turbulent portion of the boundary layer due at least in part to the change in sign of molecular oxygen production at the wall.

5. Conclusions

Direct numerical simulation of a strongly reacting hypersonic boundary layer has been performed in order to systematically characterize turbulence-aerothermochemistry inter-

actions and enable reduced-order modeling of subgrid chemistry. Within the boundary layer, the emergence of an aerodynamic heating layer gives rise to strong wall-normal variations in the chemical composition, as the bulk of the molecular oxygen dissociates within the peak-temperature location at $y^* \in [12, 13]$. While the net effect of this chemical reactivity is endothermic outside the laminar sublayer, exothermic recombination reactions prevail for $y^* < 5$, introducing considerable heat release in the vicinity of the non-catalytic wall. As the the characteristic timescales of the chemical reactivity are comparable to that of turbulent motion with $Da^t_O, Da^t_N \sim \mathcal{O}(1)$, the impact of turbulence-induced thermodynamic fluctuations on the chemical production rates is significant. Detailed characterization of and modeling for the subgrid chemical production arising due to turbulence-chemistry interactions is presented by Williams (2023). Future efforts will focus particularly on *a-posteriori* evaluation of wall-modeled large-eddy simulation of the turbulent hypersonic boundary layer presented herein (Cogo *et al.* 2023).

Acknowledgments

C.T.W. acknowledges support from the National Science Foundation Graduate Research Fellowship Program under grant DGE-2146755. This investigation was funded by the Advanced Simulation and Computing (ASC) program of the US Department of Energy's National Nuclear Security Administration (NNSA) via the PSAAP-III Center at Stanford, Grant No. DE-NA0003968. The authors thank Henry Collis for his careful review of this manuscript.

REFERENCES

Bird, R.B., Steward, W.E., & Lightfoot, E.N. 1960 *Transport Phenomena*. Wiley.

Candler, G. V. 2019 Rate effects in hypersonic flows. *Annu. Rev. Fluid Mech.* **5**, 379–402.

Cogo, M., Williams, C. T., Griffin, K.P., F. Picano, & Moin, P. 2023 Inverse-velocity transformation wall model for reacting turbulent hypersonic boundary layers. *Annual Research Briefs,* Center for Turbulence Research, Stanford University, in press

Curtiss, C.F. & Hirschfelder, J.O. 1949 Transport properties of multicomponent gas mixtures. *J. Chem. Phys.* **6**, 550–555.

Di Renzo, M., Fu, L. & Urzay, J. 2020 HTR solver: An open-source exascale-oriented task-based multi-GPU high-order code for hypersonic aerothermodynamics. *Comput. Phys. Commun.* **255**, 107262.

Di Renzo, M. & Urzay, J. 2021 Direct numerical simulation of a hypersonic transitional boundary layer at suborbital enthalpies. *J. Fluid Mech.* **912**, A29.

Duan, L. & Martín, M.P. 2011a Direct numerical simulation of hypersonic turbulent boundary layers. Part 4. Effect of high enthalpy. *J. Fluid Mech.* **684**, A3.

Duan, L. & Martín, M.P. 2011b Assessment of turbulence-chemistry interaction in hypersonic turbulent boundary layers. *AIAA J.* **49**, 172–184.

Griffin, K. P., Fu, L. & Moin, P. 2021 Velocity transformation for compressible wall-bounded turbulent flows with and without heat transfer. *P. Natl. Acad. Sci USA* **118**.

Liñán, A. & Da Riva, I. 1962 Chemical nonequilibrium effects in hypersonic aerodynamics. Tech. Rep. AD0294638. Defense Technical Information Center.

Martín, M.P. & Candler, G.V. 2001 Temperature fluctuation scaling in reacting boundary layers. AIAA Paper 2001-2717.

McBride, B.J., Zehe, M.J. & Gordon, S. 2002 NASA Glenn coefficients for calculating thermodynamic properties of individual species. Tech. Rep. 2002-211556. NASA.

Park, C. 1989 A review of reaction rates in high temperature air. AIAA Paper 1989-1740.

Park, C. 1990 *Nonequilibrium Hypersonic Aerothermodynamics*. Wiley.

Peters, N. & Warantz, J, eds. 1982 Numerical Methods in Laminar Flame Propagation: A GAMM-Workshop. Springer.

Mathur, S., Tondon, P.K. & Saxena, S.C. 1967 Thermal conductivity of binary, ternary and quaternary mixtures of rare gases *Mol. Phys.* **12**, 569–579.

Seror, S., Zeitoun, D.E., Brazier, J.P. & Schall, E. 1997 Asymptotic defect boundary layer theory applied to thermochemical non-equilibrium hypersonic flows. *J. Fluid Mech.* **339**, 213–238.

Urzay, J. 2018 Supersonic combustion in air-breathing propulsion systems for hypersonic flight. *Annu. Rev. Fluid Mech.* **50**, 593–627.

Urzay, J. & Di Renzo, M. 2020 Engineering aspects of hypersonic turbulent flows at suborbital enthalpies. *Annual Research Briefs,* Center for Turbulence Research, Stanford University, pp. 7–32.

van Driest, E. 1956 The problem of aerodynamic heating. *Aero. Eng. Rev.* **15**, 26–41.

Vincenti, W. G. & Kruger C. H. 1965 *Introduction to Physical Gas Dynamics*. Wiley.

Wilke, C.R. 1950 A viscosity equation for gas mixtures. J. Chem. Phys. **18**, 517–519.

Williams, C. T. 2023 Subgrid-scale modeling of turbulence-chemistry interaction for hypersonic boundary layers in chemical nonequilibrium. *Annual Research Briefs,* Center for Turbulence Research, Stanford University, in press

Williams, C. T., Di Renzo, M., & Moin, P. 2022 Computational framework for direct numerical simulation of shock-turbulence interaction in thermochemical nonequilibrium. *Annual Research Briefs,* Center for Turbulence Research, Stanford University, pp. 203–216.

Williams, C. T., Di Renzo, M., Moin, P. & Urzay, J. 2021 Locally self-similar formulation for hypersonic laminar boundary layers in thermochemical nonequilibrium. *Annual Research Briefs,* Center for Turbulence Research, Stanford University, pp. 119–128.